Numerical modeling of particle motion in traveling wave solar panels cleaning device

Ayyoub Zouaghi, Noureddine Zouzou

Version of Record: https://www.sciencedirect.com/science/article/pii/S0304388621000036
Manuscript_b04ede5ccf7712cc931754214cee661a

Numerical Modeling of Particle Motion in Traveling Wave Solar Panels Cleaning Device

Ayyoub Zouaghi [1*], Noureddine Zouzou [2]

[1] Laboratoire Ampère, École Centrale de Lyon, 69134 Ecully, France

[2] Institut PPRIME, CNRS, Université de Poitiers, ISAE-ENSMA, 86073 Poitiers, France

[*]Corresponding author: ayyoub.zouaghi@ec-lyon.fr

ABSTRACT

One of the promising solutions of dust accumulation on solar panels consists of using electric potential waves to prevent dust adhesion and to remove the dust layer. This study aims to understand the particle motion mechanisms on an electrostatic traveling wave conveyor. Understanding the effect of the operating parameters on particle trajectories and displacement distance is an essential step to improve the efficiency of this device and to understand the factors that can limit its performance. A numerical model that takes into account Coulomb force, dielectrophoretic, and image forces, but also gravity, drag force, and Van der Waals adhesion force is carried out. The effect of rotating electric field, frequency, and electric potential harmonics on the particle trajectories and their characteristics are analyzed and discussed. The results reveal that the particles move according to four main movement modes. The frequency is a key parameter to control particle velocity and displacement. A hyper-synchronous movement where particles reach velocities much higher than the propagation velocity of the traveling wave has been obtained under certain conditions.

KEYWORDS: numerical modeling, traveling wave, electric field, electrostatic forces, dielectric particles, displacement velocity, motion modes

1. INTRODUCTION

One of the main factors that can cause a drastic drop in the energy produced by photovoltaic (PV) panels and solar concentrators is the accumulation of dust and sand particles on their surfaces [1–3]. Finding an efficient and economical solution to avoid the problem of soiling of solar panels remains a major challenge for the scientific community in the field of solar energy [4,5]. The elimination of particles from solar panels by electrostatic forces using electrostatic traveling waves has become more widespread in recent years. The concept of electric curtain has been introduced by Masuda in the seventies [6–8], mainly for electrophotography. Then in the last twenty years, the transparent Electrodynamic Dust Shield has been developed for solar panels cleaning [9,10]. This device is so advantageous because it is simple, scalable and it doesn't require water resources to remove dust particles. Moreover, the absence of mechanical moving parts reduces considerably maintenance costs. It is also a technology that requires very low energy consumption, which can be supplied using the panel itself. The research works on the efficiency of this device on solar panels show promising results in both space [11–13] and terrestrial applications [14–16].

Theoretical and numerical studies of the traveling wave electrostatic conveyors are necessary to better understand the mechanisms of movement of particles, and to optimize the functioning of the system. Masuda et al. [6,17,18] conducted, in the 1970s and 1980s, several theoretical studies to understand the behavior of particles during experimental observations. In their early work [6], authors simulated numerically the trajectory of particles in an aerosol containment and transport system. This system consists of several ring-shaped electrodes installed in parallel forming a channel in which the charged aerosols are confined and transported by standing or traveling waves. In their model, Masuda et al. adapted a linear approximation of the motion equation, assuming small amplitude of particles oscillation. They decomposed the motion of the particles into a component of slow motion and a

component of fast oscillatory motion. In another work, Masuda et al. [18] have studied theoretically the displacement of particles on a 3-phase conveyor with sine waves. The existence of spatial harmonics has been demonstrated in the modeling of electric potential. Indeed, in the case of a conveyor with 3 or more phases, the geometry of the electrodes, most often rectangular, means that the spatial distribution of the electric potential is not perfectly sinusoidal, in particular near the surface. Therefore, electric potential is described as the infinite sum of sine waves called spatial harmonics. Masuda et al. [18] have shown that the first two harmonics, which are the more influential, propagate in two opposite directions. At the end of the 90s, Machowski and Balachandran [19] carried out a modeling of the particle trajectories, but also a study on the harmonic waves of the electric potential and their variation according to several parameters. They showed that the amplitude of the harmonics can be controlled by the geometry of the electrodes and the ratio between the width of the electrodes and the gap.

Melcher et al. [20–22] studied the trajectories and velocities of particles theoretically by developing a model of a 6-phase conveyor. In this system, the traveling wave is produced by six sources of sinusoidal voltages phase-shifted by $2\pi / 6$. The electrodes are covered with a dielectric barrier. The forces considered in this model are: the Coulomb force, the gravity force, the image force, and the drag force. However, this model does not take into account the dielectrophoretic force and the adhesion forces, in particular the van der Waals force which, according to numerous studies, have considerable values and can affect the movement of particles [23,24]. It has been shown that particles move in three main modes, which affect considerably the trajectories and velocities of particles. The first one, called “synchronous hopping mode”, appears at low frequencies. The second and third modes are asynchronous hopping and asynchronous curtain modes which can be obtained at higher frequencies. Kober [25–27] focused in his work on conductive toner particles displacement for electrophotography applications. He conducted a series of numerical studies of particles

trajectories and velocity under different square waveforms. The numerical results were in a good agreement with the experimental ones. He mentioned that smaller toner particles with a higher conductivity travel faster. Moreover, they are more subjected to higher harmonic potential waves. As a consequence, they can travel faster than the fundamental wave.

From the 2000s, one can find more experimental works than numerical ones. This trend has been reinforced by the multitude of possible applications, in particular in the field of photovoltaic energy. Nevertheless, it is possible to find some interesting models of particle trajectories under different conditions for three-phase traveling wave conveyors, some of them were validated experimentally [28–30]. Kawamoto et al. [28] used the Runge-Kutta method to solve the equation of motion and simulate particle dynamics. The forces taken into account in the model were: the Coulomb force, the dielectrophoretic force, the image force, the gravity force, and the drag force. Kawamoto et al. confirmed that the Coulomb force is the predominant force compared to other forces, and that the direction of particle transport does not always coincide with that of the traveling wave. Horenstein et al. [29] analytically calculated the trajectory of a single particle on a 3-phase conveyor using a spatio-temporal solution of electric potential. The trajectories of particles of different sizes have been studied. A chaotic behavior of the particle has been observed in certain cases, especially for large particles ($d_p = 150$ µm and 300 µm). For small particles, the movement tends to be more fluid in the direction of wave propagation. Horenstein et al. insist that a small change in the starting point of the particle can radically change its trajectory.

Zhang Jie et al. [30] also used an analytical solution of the electric field, and integrated it into the equations of motion which was then solved numerically. The forces considered in this model are: the Coulomb force, the dielectrophoretic force, the image force, the gravity and drag forces, as well as the adhesion force of van der Waals. Zhang Jie et al. classify the movement of particles in two main modes: regular and non-regular. In the irregular motion

mode, the particle moves in a disorderly fashion, this is disadvantageous for their movement. In regular motion mode, which is more favorable for moving the particles in a given direction, several types of movement have been obtained depending on the voltage, frequency, size and charge of the particles. The conditions for obtaining the different modes have not been detailed.

These works are very relevant, but there are still several effects that have not been sufficiently studied, which leave several questions unanswered, for example: are there other motion modes of particles, in addition to those already cited in the literature? What are the parameters that can affect the modes of movement of particles? How does the speed of particles vary according to these parameters?

In this paper, a numerical modeling of the trajectories of particles in a traveling wave conveyor is carried out. The particle velocity, displacement distance, and levitation height as a function of several parameters are studied and discussed. This model takes into account not only the electrostatic forces that can affect the particle motion such as Coulomb force, dielectrophoretic, and image forces, but also gravity, drag force, and Van der Waals adhesion force.

This study aims to confirm, on the one hand, the results obtained by other studies, in particular those concerning the modes of movement of particles. On the other hand, we will focus on understanding the influence of frequency and electric potential harmonics on particle trajectory, velocity, displacement distance, and levitation height. The results are discussed and analyzed with regard to the experimental observations in previous works recently published [31,32].

In the first section of this paper, we describe the mathematical model and the hypotheses taken into account as well as the numerical algorithm used for the resolution of the equations of motion. The electric field and the forces that govern particle motion are

described. After that, a detailed study of the particle trajectories and motion modes is presented. Moreover, the evolution of the characteristics such us the average velocity of the particles, the displacement distance, and the levitation height will be studied.

2. MATHEMATICAL MODEL

In this section, the mathematical models of electric field, forces and motion equations are described in detail.

2.1. Electric field

The traveling wave conveyor (TWC) under investigation is composed of several copper electrodes ($1\ \mathrm{mm}$ in width and $35\ \mu\mathrm{m}$ in thickness), engraved in parallel on a dielectric surface of $10 \times 10\ \mathrm{cm}^2$. The electrodes are energized by a 3-phase applied voltage system. The gap spacing between the electrodes is fixed at $1\ \mathrm{mm}$, which makes the geometrical periodicity $\lambda = 6\ \mathrm{mm}$. In order to make our analysis clear, we emphasize that the forward direction is the direction of phase succession in the case of the TWC (right direction in figures). The backward direction is the opposite direction of phase succession (left direction in figures). A typical electric potential distribution in the space over the electrodes is illustrated in Figure 1. This simulation has been carried out using COMSOL Multiphysics® commercial software by resolving the Laplace's equation.

The boundary conditions on the electrodes are given by the Dirichlet type condition $V1$, $V2$ and $V3$ for the electrodes centered on the positions $x = 0\ \mathrm{mm}$, $x = 4\ \mathrm{mm}$ and $x = 6\ \mathrm{mm}$, respectively. On the other hand, Neumann conditions are fixed on the limits of space in the direction of the y axis. A periodic condition has been set on the limits of the x axis.

$$V1 = V_0 \cos(\omega t) \tag{1}$$

$$V2 = V_0 \cos\left(\omega t - \frac{2\pi}{3}\right) \tag{2}$$

$$V3 = V_0 \cos\left(\omega t - \frac{4\pi}{3}\right) \quad (3)$$

With, $V_0 = 1000\,V$ is the electric potential maximum value and ω the angular frequency (or angular speed).

In our work, an analytical model of electric potential is used to simplify the resolution of the motion equations. This model is inspired from the work of Masuda et al. [6,18] for the 3-phase configuration. However, the particularity of this study is that the electric potential function on the electrodes ($y = 0$) has been obtained by numerical simulation in order to consider the non-linearity of the electric potential between the electrodes [31]. In fact, the electrical potential wave in the 3-phase configuration is not perfectly sinusoidal because of the rectangular geometry of the electrodes. Thus, it is composed of infinity of harmonics that can be extracted using Fast Fourier Transformation (FFT). Most of harmonics are very weak in amplitude and can be neglected, except first and second order harmonics. Taking those two harmonics in consideration, the electric potential V can be expressed as the sum of two waves W_{for} and W_{back} (forward and backward waves) that propagate in two different directions [6,31]:

$$V(x,y,t) \approx W_{for} + W_{back} = V_0\left[\frac{3}{2}a_1 e^{-\frac{2\pi}{\lambda}y}\cos\left(\frac{2\pi}{\lambda}x - \omega t\right) + \frac{3}{2}a_2 e^{-\frac{4\pi}{\lambda}y}\cos\left(\frac{4\pi}{\lambda}x + \omega t\right)\right] \quad (4)$$

with, a_1 = 0,527 and a_2 = 0,228 are the first and the second Fourier coefficients of 1 phase electric potential function on the electrodes ($y = 0$). $\lambda = 6\,mm$ is the geometrical periodicity.

By solving the equation $E = -\nabla V$ analytically, we can deduce the two parts of the electric field (E_x and E_y) as a function of space and time:

$$E(x,y,t) = \begin{pmatrix} E_x(x,y,t) \\ E_y(x,y,t) \end{pmatrix} \approx \begin{pmatrix} V_0\left[\frac{3\pi}{\lambda}a_1 e^{-\frac{2\pi}{\lambda}y}\sin\left(\frac{2\pi}{\lambda}x-\omega t\right)+\frac{6\pi}{\lambda}a_2 e^{-\frac{4\pi}{\lambda}y}\sin\left(\frac{4\pi}{\lambda}x+\omega t\right)\right] \\ V_0\left[\frac{3\pi}{\lambda}a_1 e^{-\frac{2\pi}{\lambda}y}\cos\left(\frac{2\pi}{\lambda}x-\omega t\right)+\frac{6\pi}{\lambda}a_2 e^{-\frac{4\pi}{\lambda}y}\cos\left(\frac{4\pi}{\lambda}x+\omega t\right)\right] \end{pmatrix} \quad (5)$$

The system of equations (5) indicates that the electric field (on x or y) is made up of two dominant components, one component linked to the forward wave (E_{for-x} or E_{for-y}) and another component linked to the backward wave (E_{back-x} or E_{back-y}) of electric potential. Knowing that $\alpha = \frac{2\pi}{\lambda}$ and $E_0 = \alpha V_0$, the two components are given by the equations:

$$\begin{cases} E_{for-x}(x,y,t) \approx E_0\left[\frac{3}{2}a_1 e^{-\alpha y}\sin(\alpha x-\omega t)\right] \\ E_{for-y}(x,y,t) \approx E_0\left[\frac{3}{2}a_1 e^{-\alpha y}\cos(\alpha x-\omega t)\right] \end{cases} \quad (6)$$

$$\begin{cases} E_{back-x}(x,y,t) \approx E_0\left[\frac{6}{2}a_2 e^{-2\alpha y}\sin(2\alpha x+\omega t)\right] \\ E_{back-y}(x,y,t) \approx E_0\left[\frac{6}{2}a_2 e^{-2\alpha y}\cos(2\alpha x+\omega t)\right] \end{cases} \quad (7)$$

Those equations indicate that the electric field, at a point in the space (x, y), is given by the superposition of two components which rotate as a function of time, but in two different directions. Figure 2 shows the evolution of the electric field vectors and its forward and backward components as a function of time at some specified points above the electrodes. The points have the coordinates (x, y): (5, 0.1), (5.5, 0.1), and (6, 0.1) mm. The first point is located between the electrodes, the second is located at the edge, and the third point is located in the middle of the electrode. The electric field vectors are given at different times starting from $t = 0$ s, the direction of rotation is indicated in green in the figures. These results show that as a function of time the total electric field and its forward component rotate counterclockwise, while the backward component of the electric field rotates clockwise. It should be noted that the two components rotate with the same angular speed ω. The vectors of the electric field form a circular geometry for the two forward and backward components because of the perfectly sinusoidal electric potential waves; while the combination of these

components gives a rather extensive elliptical shape. Moving on the axis (Ox) from $x = 5$ mm to $x = 6$ mm, the axis of the ellipse rotates clockwise, keeping the same dimensions of the ellipse. The following sections will show that the rotating electric field affects greatly the movement of particles.

2.2. Equations of motion

The forces taken into account in this model for the calculation of particle trajectory are: the Coulomb force, the dielectrophoretic force, the image force, the drag force, the gravity force, and the adhesion force of Van der Waals. The latter only intervenes in the model if the particle is in contact with the surface.

The Coulomb force $\overrightarrow{F_c}$ is responsible for particles motion initiation because it is the only repelling force that can have a positive vertical component with considerable value [28,23,24]. It is proportional to the particle charge q_p and electric field:

$$\overrightarrow{F_c} = q_p \cdot \vec{E} \tag{8}$$

In order to move particles using TWC, they have to be charged. This charge can be acquired through different mechanisms such as tribo-electric and field charging. Thus, the charge of particles cannot be predicted theoretically with precision, since it depends on different parameters such as the surface state, the material and the size of the particles, the surface state of the conveyor, the inter-particle collisions, the space charge, the electric field value, among others. However, there is a simple theoretical model to estimate the maximum charge a particle can carry. This maximum charge is limited by the breakdown of air when the electric field at the surface of the particle reaches the critical value [33]. This charge of saturation q_{ps} can be calculated by the relation of Pauthenier [34]:

$$q_{ps} = 4\pi {r_p}^2 \varepsilon_0 \frac{3\varepsilon_{rp}}{\varepsilon_{rp} + 2} E_0 \tag{9}$$

where, ε_0 and ε_{rp} the dielectric permittivity of vacuum and the relative permittivity of the particles respectively. E_0 is the dielectric strength of air ($E_0 \approx 3 \times 10^6$ V/m).

The dielectrophoretic force (or DEP force) $\overrightarrow{F_{DEP}}$ results from the interaction between the non-uniform electric field and the dipole moment induced in a dielectric particle [35,36]. It is given by the equation:

$$\overrightarrow{F_{DEP}} = 2 \cdot \pi \cdot {r_p}^3 . \varepsilon_0 . \varepsilon_{rm} \cdot \frac{\varepsilon_{rp} - \varepsilon_{rm}}{\varepsilon_{rp} + 2\varepsilon_{rm}} \cdot \nabla(E^2) \quad (10)$$

Where, r_p is the particle's radius. ε_{rp} and ε_{rm} are the relative permittivities of the particle and the medium respectively. In this simulation, spherical PMMA particles are considered with $\varepsilon_{rp} = 3.2$.

The image force $\overrightarrow{F_{img}}$ exerted on a particle placed at a distance y_p from a metallic surface can be given by the relation [37]:

$$\overrightarrow{F_{img}} = -\frac{{q_p}^2}{4\pi\varepsilon_0(2y_p)^2}\vec{\mathbf{n}} \quad (11)$$

Where $\vec{\mathbf{n}}$ the normal vector perpendicular to the surface and oriented towards the particle.

The drag force $\overrightarrow{F_D}$, which describes the friction between a spherical particle and the gas, is given by Stokes relation [38]:

$$\overrightarrow{F_D} = 6\pi . \eta_g . r_p . \left(\overrightarrow{U_g} - \overrightarrow{v_p}\right) . \frac{1}{Cu(r_p, \lambda_g)} \quad (12)$$

In this equation, $\eta_g = 1{,}85 \times 10^{-5}$ kg. m^{-1}. s^{-1} is the dynamic viscosity of the air. $\overrightarrow{U_g}$ is the velocity of the flow, and $\overrightarrow{v_p}$ is the velocity of the particle. In this study, we assume that the air is in a static state, so its velocity drops to zero. If the particle size is comparable to the mean free path λ_g of the gas molecules, the particles will move in a discontinuous medium

and the Cunningham factor Cu must be introduced in the equation. In our case, the particle size is a few orders of magnitude greater than the mean free path, therefore, $\mathrm{Cu} = 1$.

The gravity force $\overrightarrow{F_g}$ equation is given by:

$$\overrightarrow{F_g} = m_p . \vec{g} = \frac{4}{3}\pi {r_p}^3 . \rho . \vec{g} \tag{13}$$

Where, m_p and ρ are respectively the mass and the density of the particle material which is PMMA and $\vec{g}$ the gravity acceleration vector.

The Van der Waals force $\overrightarrow{F_{vdW}}$ is an adhesion force exerted on a particle when it is in contact with the surface. When the surfaces of the particle and the substrate are perfectly smooth, the force is given by the relation [39]:

$$\overrightarrow{F_{vdW}} = -\frac{A_h r_p}{6D^2}\vec{\mathbf{n}} \tag{14}$$

with, A_h the Hamaker constant (of the order of 10^{-19} J in vacuum) and D the shortest distance between the particle and the substrate (of the order of 10^{-10} m).

In a practical case, the surfaces of the particle and the substrate contain asperities. Therefore, the surface roughness can considerably influence the adhesion strength. According to Rabinovich et al. [40], the adhesion force between a smooth particle and a surface with nanometric roughness can be expressed by:

$$\overrightarrow{F_{vdW}} = -\frac{A_h r_p}{6D^2} \cdot \left[\frac{\gamma^2}{\gamma^2 + 58{,}14 r_p \cdot \mathrm{RMS}} + \frac{D^2}{(D + 1{,}817 \cdot \mathrm{RMS})^2}\right]\vec{\mathbf{n}} \tag{15}$$

with, RMS the quadratic mean value of the surface roughness (≈ 3 nm) and γ the mean distance between the peaks of the asperities (≈ 20 nm) [40,41]. In this approach, the first term in square brackets represents the contact interaction of the particle with an asperity and the second term represents the contactless interaction of the particle with an average surface plane [40,41].

To simplify the problem, we have considered the following assumptions:

- The resolution of the problem is made in two dimensions; we consider that there is no movement on the axis (Oz).
- There is no charge exchange when a particle touches the surface of the conveyor, the particle retains its initial charge during movement.
- The simulation is carried out for one single particle assuming that the mechanical and electrical interactions between particles are neglected.
- An elastic collision condition is taken into account at the surface with a restitution coefficient equal to 1. This means that when the particle bounces on the surface, its speed along the normal axis is reversed: $v_{y-after} = -v_{y-before}$
- The thickness of the electrodes is negligible and there is no dielectric barrier.

The system of equations solved in this modeling is as follows:

$$\begin{cases} m_p \frac{d^2x_p}{dt^2} + 6\pi\eta_g r_p \frac{dx_p}{dt} = q_p E_x(x_p, y_p, t) + 4\pi {r_p}^3 . \varepsilon_0 . \frac{\varepsilon_{rp} - 1}{\varepsilon_{rp} + 2} \left[E_x(x_p, y_p, t) \frac{\partial E_x(x_p, y_p, t)}{\partial x_p} + E_y(x_p, y_p, t) \frac{\partial E_y(x_p, y_p, t)}{\partial x_p} \right] \\ m_p \frac{d^2y_p}{dt^2} + 6\pi\eta_g r_p \frac{dy_p}{dt} = q_p E_y(x, y_p, t) + 4\pi {r_p}^3 . \varepsilon_0 . \frac{\varepsilon_{rp} - 1}{\varepsilon_{rp} + 2} \left[E_x(x, y_p, t) \frac{\partial E_x(x, y_p, t)}{\partial y_p} + E_y(x, y_p, t) \frac{\partial E_y(x, y_p, t)}{\partial y_p} \right] \\ -m_p g - \frac{{q_p}^2}{4\pi\varepsilon_0 (2y_p)^2} - \frac{A_h r_p}{6D^2} \cdot \left[\frac{\gamma^2}{\gamma^2 + 58.14 r_p \cdot RMS} + \frac{D^2}{(D + 1.817 \cdot RMS)^2} \right] . \delta(y - r_p) \end{cases} \quad (16)$$

x_p and y_p are the coordinates of the position of the particle. $\delta(y_p - r_p)$ is a function, given by :

$$\delta(y_p - r_p) = \begin{cases} 1 \text{ if } y_p = r_p \text{ (Particle on the surface)} \\ 0 \text{ else} \end{cases} \quad (17)$$

Solving a system of 2nd order differential equations directly is complicated. To simplify the resolution, it is preferable to decompose it into a system of four 1st order equations:

$$\begin{cases} v_x = \dfrac{dx_p}{dt} \\ a_x = \dfrac{d^2x_p}{dt^2} = -T\dfrac{dx_p}{dt} + C.E_x(x_p, y_p, t) + D.\left[E_x(x_p, y_p, t)\dfrac{\partial E_x(x_p, y_p, t)}{\partial x_p} + E_y(x_p, y_p, t)\dfrac{\partial E_y(x_p, y_p, t)}{\partial x_p}\right] \\ v_y = \dfrac{dy_p}{dt} \\ a_y = \dfrac{d^2y_p}{dt^2} = -T\dfrac{dy_p}{dt} + C.E_y(x_p, y_p, t) + D.\left[E_x(x_p, y_p, t)\dfrac{\partial E_x(x_p, y_p, t)}{\partial y_p} + E_y(x_p, y_p, t)\dfrac{\partial E_y(x_p, y_p, t)}{\partial y_p}\right] \\ -g - W.\delta(y_p - r_p) - M.\dfrac{1}{{y_p}^2} \end{cases} \tag{18}$$

where, (v_x, v_y) and (a_x, a_y) are the velocity and particle acceleration components on the (Ox) and (Oy) axes respectively. T, C, D, W and M are constants given by:

$$T = \frac{6\pi\eta r_p}{m_p} \tag{19}$$

$$C = \frac{q_p}{m_p} \tag{20}$$

$$D = \frac{4\pi {r_p}^3}{m_p}.\varepsilon_0.\frac{\varepsilon_{rp} - 1}{\varepsilon_{rp} + 2} \tag{21}$$

$$W = \frac{1}{m_p}.\frac{A_h r_p}{6D^2}\left[\frac{\gamma^2}{\gamma^2 + 58.14 r_p \cdot RMS} + \frac{D^2}{(D + 1.817 \cdot RMS)^2}\right] \tag{22}$$

$$M = \frac{{q_p}^2}{16\pi\varepsilon_0 m_p} \tag{23}$$

The system of equations is solved using a code on MATLAB® that employs fourth order Runge-Kutta method (RK4). The calculation procedure is summarized as follows: the algorithm begins with the declaration of constant parameters and initial conditions at t_0. It is also necessary to define the time step Δt as well as the end time t_{end}. In this study, the particle trajectories are calculated during 1 s. The time step is initially set at 10^{-6} s, but this time step may vary in the next iteration depending on the results of the particle displacement. The system of differential equations is then solved for the next moment $t_0 + \Delta t$ using the RK4 method. After checking the rebound condition on the surface, a new iteration is carried out. The calculation therefore stops when the calculation time reaches $t_{end} = 1$ s. The last step consists in displaying the results and calculating the characteristic parameters of the

trajectories such as the maximum levitation height (y_{max}), the displacement distance (d), the maximum velocity reached by the particle along the axis (Ox) (v_{x-max}), and the average transportation velocity (v_{x-avg}).

3. SPATIAL DISTRIBUTION OF THE ACCELERATION

Before studying the trajectories of particles, the distribution of acceleration in space is analyzed in this section. The acceleration is given by the sum of all the forces exerted on a particle divided by its mass. Figure 3 presents the 2D distributions of the two components of the acceleration a_x and a_y at time $t_0 = 0$ s. In this simulation, the PMMA particle diameter is fixed at 60 µm and its charge is at 10 % of the total saturation charge q_{ps} (positive polarity). This charge value has been chosen based on experiments. Measurements of the charge/mass ratio of displaced PMMA particles have been carried out experimentally using a Faraday cup and electrometer. Assuming that the particles charge is monopolar, and knowing the density of PMMA material, the charge of one single particle can be calculated approximately. The results show that the displaced PMMA particles carry a positive charge that can reach 10 % q_{ps}. The particle in this simulation is considered to be in a static state, which means that its velocity is zero. The centers of the electrodes are located at the points $x = 0, 2, 4, 6, 8, 10$ and 12 mm. The positive acceleration in a given position indicates that the movement of the particle will take place in the forward direction. It should be noted that the horizontal component of the acceleration a_x is zero on the axis perpendicular to the midpoints of the electrodes because of the symmetry of the electric potential at this time. The vertical component is positive on the electrode under positive electric potential ($x = 0$, 6, and 12 mm), and it is negative on the rest of the surface. The most favorable position for triggering the movement of particles toward the forward direction is when the two components of the acceleration are positive. Particles can begin their movement by moving in

the opposite direction if the vertical component is positive while the horizontal component is negative.

4. PARAMETRIC STUDY OF PARTICLE TRAJECTORIES

In this part, we analyze the trajectories of the particles as a function of different factors such as: the applied voltage, the frequency, the size and the charge of the particles. The aim is to characterize the different modes of movement of the particles and to study the effect of the different parameters on some movement characteristics such as the maximum levitation height (y_{max}), the travel distance (d), the maximum velocity reached by the particle (v_{x-max}) and the average displacement velocity (v_{x-moy}). The travel distance is calculated over a time of 1 s with this formula:

$$d = x_p(t_{end} = 1\ s) - x_0 \tag{24}$$

where $x_p(t_{end} = 1\ s)$ and x_0 are the positions of the particle at times $t_{end} = 1\ s$ and $t_0 = 0\ s$, respectively.

The calculation of the average displacement velocity is quite critical, due to the existence of several phases of movement of the particles as a function of time. In addition, it is essential to ensure that the average transport velocity does not vary considerably depending on the initial position of the particle. Figure 4 illustrates the trajectories of the particles for several starting positions at some particular instants of their movement ($10\ ms$, $50\ ms$, $100\ ms$ and $200\ ms$). These instants were chosen to illustrate the different phases of movement of the particles as a function of time.

In this simulation, the voltage and frequency are fixed at $1000\ V$ and $100\ Hz$ respectively. The particles have a diameter of $60\ \mu m$ and a positive charge of $10\ \%$ of the saturation charge q_{ps}. The particles located on the electrodes at $t = 0\ s$ jump out as soon as a positive voltage is applied, however, the particles located between the electrodes move

horizontally on the surface until they reach a zone with a high vertical electric field such as the surface of an electrode with a positive potential. On the other hand, it is possible that the particles temporarily stuck at the edges of the electrodes because of the dielectrophoretic force which dominates this area [23,24]. This phenomenon can affect negatively the movement of particles, but its effect is not significant, because the area of dominance of the dielectrophoretic force is very small [24].

One can distinguish three phases of particle movement, a levitation phase during which the particles are projected a few millimeters from the surface as soon as the voltage is applied (Figure 4.a). The levitation phase is followed by a particles-fall phase (Figure 4.b) because of the effect of gravity and negative Coulomb's force. In the third phase (Figure 4.c and Figure 4.d), the particles start moving forward toward the direction of the propagation of the electric wave. Under the conditions of this simulation, they move in rotary motion because of the rotating electric field (cf. section 2.1). The particles can also move backward in some circumstances. The modes of movement of particles will be studied in detail in the following sections.

In order to confirm those trajectories, experimental visualization of particle trajectories has been carried out. In this experiment, spherical shape PMMA particles initially deposited over the surface of the conveyor are highlighted using a high speed pulsed light LED illuminator (HARDsoft, IL-105 / 6X). Once the voltage signals are applied, the motion of the particles is visualized and recorded using high-speed camera (Photron, Fastcam SA1.1, resolution of 1024 × 1024 pixels, 5400 images per second). PMMA particles are chosen in this study mainly because they are clearly visible by the optical system. The acquisition rate is set to 1000 Hz, which allows a good analysis of the particle dynamics. The experiment is performed at atmospheric pressure and room temperature. More detailed information about the experimental setup and protocol can be obtained in [32].

Figure 5 presents the trajectories of the particles obtained experimentally. The conditions of voltage and frequency used in the experiments are similar to those of the simulation. These images were obtained by accumulating the positions of the particles during 200 ms of their movement (200 superimposed frames). Several similarities can be noticed on the trajectories obtained by simulation and those obtained experimentally. First, we can see the high jumps of the particles which appear during the levitation phase, at the beginning of their movement. The rotary movement of the particles counterclockwise is also obtained experimentally (see the zoomed area in Figure 5). The observation of this movement experimentally was difficult due to very high number of particles in our experiments. This movement is caused by the rotating electric field, analytically modeled in section 2. Similar motion mode has been observed experimentally under other conditions by Balachandran et al. [19,42] and Dudzizc et al. [43,44], who confirm our observations. The heights reached by the particles obtained by simulation are very close to those of the experiment, in which rotary trajectories at different heights can be observed. This is due to the fact that the particles have a large size distribution ($d_p[50\ \%] = 57\ \mu m$, $d_p[10\ \%] = 37\ \mu m$ and $d_p[90\ \%] = 86\ \mu m$), so the different heights may be related to particles with different sizes and/or different charges. Also, particle charge distribution can contribute to such experimental result.

The evolution of the components of the position (x_p and y_p) and the velocity (v_x and v_y) of particles deposited at different positions as a function of time is illustrated in Figure 6. The curve $x_p(t)$ (Figure 6.a) indicates that the particles follow the electric field during the levitation phase. Consequently, the particles located on the right of the positive energized electrode start moving forward ($x_p(t)$ increases), and the particles located on the left of the same electrode start moving backward ($x_p(t)$ decreases), before they return in the forward direction later because of the electric potential wave. From Figure 6.a, one can notice also that the initial position of a particle does not have a significant effect on its average velocity

calculated in the steady state. However, it has an effect on the trajectory of the particle in the transient state at the beginning of their movement.

The curve $y_p(t)$ (Figure 6.b) in the case of $x_0 = 6.3\ \text{mm}$ indicates that the particle reaches the maximum levitation height $y_{max} \approx 3.7\ \text{mm}$ at the end of the levitation phase. The curve $v_x(t)$ (Figure 6.c) shows that in the steady state, the variation of the velocity as a function of time is oscillatory with a non-zero mean value ($v_{x-moy} \approx 0.02\ \text{mm/s}$). The y component of the velocity $v_y(t)$ show also an oscillatory evolution as a function of time (Figure 6.d). The movement of particles goes through two main states: a transient state and a steady state. The transient state in this simulation lasts approximately $120\ \text{ms}$. However, the duration of this state can vary from a few milliseconds to a few hundred milliseconds depending on the parameters of the simulation (voltage, frequency, size and charge of the particles). The appearance (or not) of the different phases of movement also depends on the parameters mentioned above. The variation of particles trajectories as a function of different parameters will be presented in the following sections.

4.1. Frequency effect

The effect of frequency on the trajectory, maximum levitation height, distance crossed and the velocity of particles is studied in this section. The applied voltage is fixed at $1000\ \text{V}$, the particles have a size of $60\ \mu\text{m}$ and a positive charge of $10\%\ q_{ps}$. Figure 7 shows the variation of the maximum levitation height of the particle y_{max} and the displacement distance d as a function of the frequency. The results show that the two curves pass through a maximum. The maximum levitation height increases with frequency, it reaches its maximum value of $7.6\ \text{mm}$ at $40\ \text{Hz}$. Between $40\ \text{Hz}$ and $200\ \text{Hz}$, y_{max} decreases when the frequency increases. The same evolution is observed for the distance of displacement, its maximum value ($189\ \text{mm}$) has been obtained at $60\ \text{Hz}$. Between $60\ \text{Hz}$ and $400\ \text{Hz}$, the distance crossed by the particle drops. Above $400\ \text{Hz}$, the distance of movement takes negative values

which means that the particles start to move slightly in the opposite direction, but this distance remains very short. Despite the assumptions made in this simulation, the results obtained are in very good agreement with the experimental results of displacement efficiency presented in previous works [17,22]. Indeed, better efficiency has been obtained for a frequency of 50 Hz, and movement of particles in the opposite direction has been observed for high frequencies.

Figure 8 illustrates the variation of the time-average velocity of particles in steady state v_{x-avg} as well as the maximum speed v_{x-max} as a function of the frequency. The synchronism velocity, given by the product of the frequency and the geometric period λ, is illustrated for the comparison with a blue line. Based on the time-average velocity curve, it is possible to distinguish the two main modes of movement mentioned in the literature [20,21,28,30], **the synchronous** and **asynchronous modes**. In the synchronous mode, the particle moves horizontally with an average velocity equal to the synchronism value. This mode is obtained for frequencies less than or equal to 60 Hz. For frequencies ranging between 70 Hz and 300 Hz where the motion mode is asynchronous, the particle continues to move forward but its velocity is very low compared to the synchronism velocity. For frequencies above 400 Hz, the particle velocity is very low and it shows negative values. We can consider the movement of the particle for this frequency range as a separate mode, we call it **backward motion mode**. The curve of the maximum instantaneous velocity (green line) indicates that the particle can reach much higher velocities than the synchronism velocity for frequencies less than or equal to 60 Hz. For example, at 10 Hz, the particle can exceed 0.6 m/s during its movement, while the synchronism velocity for this frequency is limited to 0.03 m/s. This confirms the experimental observations already made in a previous study [45]. However, hyper-synchronous motion is not considered as a separate mode because the average particle velocity calculated in the steady state is equal to the synchronism value for

these frequencies. **Hyper-synchronous motion** doesn't exist for frequencies above 60 Hz, since the maximum instantaneous velocity is lower than the synchronism value.

Figure 9 illustrates the variation of the particle's position and the horizontal component of the particle's instantaneous velocity as a function of time during the 200 ms following the application of the voltage. During the first 60 ms, one can notice that the particle is in **hyper-synchronous motion**. The **hyper-synchronous motion** appears at low frequencies during the transient state of the particle's movement, for which the particle is pushed by the Coulomb force for long distances with high velocities. For low frequencies, the instantaneous velocity of the particle is very fluctuating during time. At a given instant, its value is either higher or lower than the synchronism velocity, but its time average value is equal to the synchronism velocity. Since the particles have a hyper-synchronous movement at the beginning of the synchronous mode, low frequencies are more favorable for particles velocity control and for obtaining better displacement efficiency.

Figure 10 represents the trajectories of one single particle for different frequency values between 5 Hz and 500 Hz, those trajectories are calculated for a duration of 1 s. The results show that the trajectories are very sensitive to the frequency. At 5 Hz for example, the movement of the particle begins with a hyper-synchronous movement which lasts approximately 60 ms; then the particle slides on the surface in synchronous mode. A similar dynamic is obtained for a frequency of 20 Hz, except that the duration of the hyper-synchronous movement is very short, since the particle quickly passes to a **hopping synchronous mode**. Those trajectories are in agreement with trajectories in literature [20,21,28,30]. In this case, the particle moves by making jumps above the surface with a horizontal instantaneous velocity that oscillates around the synchronism value. At 50 Hz, the particles move in hopping synchronous mode, the height of the jumps is bigger. The mechanism in this mode is as follows: the positively charged particles are pushed by the

Coulomb force when they are on an electrode with a positive potential; then, they fall down towards the surface under the influence of multiple attracting forces. At 100 Hz, the particle moves in asynchronous mode, its time-average velocity is much lower than the synchronism velocity as previously illustrated in Figure 8. In this mode, the particle has a rotary motion and remains suspended in the air in steady state. The particle is pushed up by positive Coulomb force during the first half-cycle, and then it falls down during the negative half-cycle. However, it doesn't have enough time to return back to the surface because of the period is very short at high frequency. The next positive half-cycle comes quickly and pushes it up again before it touches the surface. This **rotary asynchronous mode** can be found in the literature under the names "curtain mode" [20,21,28,30]. The rotary asynchronous mode is also obtained at 200 Hz but with a lower height and smaller distance of displacement. At 500 Hz, a movement in the opposite direction over a very short distance (less than 1 mm) can be observed. However, the horizontal movement stops quickly and the particle only makes vibrations and small jumps without significant displacement, this movement can be considered as a separate mode which is called **vibratory mode**. In the latter mode, the time-average velocity of the particle in the steady-state oscillates around a zero mean value.

4.2. Potential harmonics effect

In this part, the effect of the electric potential harmonics on the movement of the particles is studied. In our knowledge, this study has not been previously reported in the literature. A comparative study of the trajectories, displacement distances as well as average particle velocity between three cases was carried out. The first case takes into account the total electric field (the same case as the previous section). In the second case, the simulation only takes into account the electric field created by the direct potential wave given by equation (6). In the third case, only the electric field created by the backward potential wave is taken into account, the analytical equation of the spatio-temporal variation of the field of

the backward wave is given by equation (7). Typical particle trajectories for the three cases are shown in Figure 11. The conditions of the voltage, the frequency and the charge of the particles are: $1000\ \mathrm{V}$, $100\ \mathrm{Hz}$, and $10\%\ q_{ps}$ respectively. Two cases are simulated here, a case where the particles move forward (obtained for $d_p = 60\ \mu\mathrm{m}$), and a case where the particles move backward (obtained for $d_p = 320\ \mu\mathrm{m}$). In the first case (Figure 11.a), under the effect of the forward wave, the particle moves forward with rotary asynchronous mode. On the other hand, when we apply only the backward wave, the particle moves backward with a different mode, similar to the hopping synchronous mode. In the second case (Figure 11.b), when both forward and backward waves are taken into account, the particle moves backward. But once the contribution of the backward wave is neglected, the particles move forward (curve in red). These results confirm that the backward potential harmonics are the main reason of the particles movement in the opposite direction. In Figure 11.b, we note that the mode of movement is the same for the three cases, and that the maximum levitation height for the backward wave case is lower than that obtained with the other cases. This can be explained by the fact that the amplitude of the backward potential wave is lower than that of the forward wave.

Figure 12 illustrates the variation of the displacement distance as a function of the frequency for the three cases. The results are obtained for a particle of $60\ \mu\mathrm{m}$ in diameter. In the case where only the forward wave is considered (curve in red), the evolution is similar to the result obtained with both forward and backward waves (curve in black), but with a greater distance of displacement between $20\ \mathrm{Hz}$ and $60\ \mathrm{Hz}$. The distance reaches $248\ \mathrm{mm}$ for the case of the forward wave, and does not exceed $180\ \mathrm{mm}$ for the case of the sum of forward and backward cases. The optimal frequency, for which the displacement distance is maximal, is around $50\ \mathrm{Hz}$ in the case of the forward wave, and $60\ \mathrm{Hz}$ in the case of the sum of forward + backward waves. One can notice that there is a small backward displacement at high

frequencies because of the contribution of the backward wave. In the case when only the backward wave is applied (curve in blue), the particle moves backward. The displacement distance increases linearly with frequency up to $100\,\mathrm{Hz}$, before it drops for higher frequencies.

Figure 13 shows the evolution of the average displacement velocity as a function of frequency for the three cases. The results confirm the trends obtained with the displacement distance. The optimal frequency, where the average velocity reaches its maximum value, is around $50\,\mathrm{Hz}$ in the case of the forward wave and $100\,\mathrm{Hz}$ in the case of the backward wave. This may be explained by the fact that the propagation speed of the backward wave is half the speed of the forward wave. However, the maximum velocity of movement reached as a function of the frequency is the same in both directions when only one wave is applied; it is equal to $0.3\,\mathrm{m/s}$.

5. CONCLUSION

This work aims to understand the mechanisms that control the particle motion in traveling wave solar panels cleaning devices. A numerical code has been implemented by taking into account six forces: the drag force, the gravity force, the Coulomb force, the dielectrophoretic force, the image force, and the adhesion force of Van der Waals. The main results can be summarized as follows:

The movement of particles as a function of time goes through a transient state and a steady state. In the transient state, three phases of particle movement have been identified: a levitation phase, followed by a particle fall phase, then an acceleration phase. In the steady state, the instantaneous velocity of the particle as a function of time oscillates around an average value less than or equal to the synchronous value depending on the experimental conditions.

The initial position of the particle does not have a significant effect on the average velocity of the particle in steady state, but it can largely affect the initiation of movement.

The frequency effect analysis allows us to distinguish four main movement modes. The first is the hopping synchronous mode for which the average particle velocity increases linearly with frequency. The asynchronous mode has two types: hopping and rotary. In both, the particles move forward with a speed lower than the synchronism velocity. The rotary movement is due to the fact that the electric field at a given point in space is rotary. The direction of rotation can be reversed by reversing the sequence of the phases. The vibratory mode is characterized by an instantaneous speed of the particles which oscillates around a zero mean value. Finally, there is the backward motion mode, which appears at high frequency. This mode is mainly caused by the backward harmonic wave.

A hyper-synchronous movement appears at low frequencies during the transient state of movement of the particles. Here, the particles are pushed by the Coulomb force with a velocity which can greatly exceed the synchronism velocity.

In order to improve the efficiency of electrostatic conveyors, we need to improve the displacement velocity of particles. This last can be increased by increasing the propagation velocity of the forward traveling potential wave which is proportional to frequency. The particle velocity and displacement distance go through a maximum as a function of frequency. Thus, choosing the optimal frequency value is necessary. Eliminating the backward potential wave can also help to get a better efficiency.

Further investigations are necessary to understand more clearly the behavior of micrometer sized particles under the effect of a travelling wave electric potential. The numerical modelling could include the non-uniformity of the particles shape, charge and size, the particle-particle and particles-substrate interactions, the exchange of the electric charge before and after collision, and the 3D motion of particles.

ACKNOWLEDGEMENTS

The authors would like to thank the French Ministry of Higher Education, Research and Innovation (M.E.S.R.I.) for the financial support.

REFERENCES

[1] A. Sayyah, M.N. Horenstein, M.K. Mazumder, Energy yield loss caused by dust deposition on photovoltaic panels, Solar Energy. 107 (2014) 576–604. https://doi.org/10.1016/j.solener.2014.05.030.

[2] F.M. Zaihidee, S. Mekhilef, M. Seyedmahmoudian, B. Horan, Dust as an unalterable deteriorative factor affecting PV panel's efficiency: Why and how, Renewable and Sustainable Energy Reviews. 65 (2016) 1267–1278. https://doi.org/10.1016/j.rser.2016.06.068.

[3] M.R. Maghami, H. Hizam, C. Gomes, M.A. Radzi, M.I. Rezadad, S. Hajighorbani, Power loss due to soiling on solar panel: A review, Renewable and Sustainable Energy Reviews. 59 (2016) 1307–1316. https://doi.org/10.1016/j.rser.2016.01.044.

[4] T. Sarver, A. Al-Qaraghuli, L.L. Kazmerski, A comprehensive review of the impact of dust on the use of solar energy: History, investigations, results, literature, and mitigation approaches, Renewable and Sustainable Energy Reviews. 22 (2013) 698–733. https://doi.org/10.1016/j.rser.2012.12.065.

[5] D. Deb, N.L. Brahmbhatt, Review of yield increase of solar panels through soiling prevention, and a proposed water-free automated cleaning solution, Renewable and Sustainable Energy Reviews. 82 (2018) 3306–3313. https://doi.org/10.1016/j.rser.2017.10.014.

[6] S. Masuda, K. Fujibayashi, K. Ishida, H. Inaba, Confinement and transportation of charged aerosol clouds via electric curtain, Electrical Engineering in Japan. 92 (1972) 43–52. https://doi.org/10.1002/eej.4390920106.

[7] S. Masuda, Apparatus for electric field curtain of contact type, US3778678A, 1973. https://patents.google.com/patent/US3778678A/en?oq=US3778678 (accessed July 23, 2019).

[8] S. Masuda, Booth for electrostatic powder painting with contact type electric field curtain, US3801869A, 1974. https://patents.google.com/patent/US3801869A/en?oq=US3801869 (accessed July 23, 2019).

[9] M. Mazumder, R. Sims, J. Wilson, Transparent self-cleaning dust shield, US20040055632A1, 2004. https://patents.google.com/patent/US20040055632A1/en (accessed December 7, 2018).

[10] M.K. Mazumder, R. Sharma, A.S. Biris, J. Zhang, C. Calle, M. Zahn, Self-cleaning transparent dust shields for protecting solar panels and other devices, Particulate Science and Technology. 25 (2007) 5–20. https://doi.org/10.1080/02726350601146341.

[11] C.I. Calle, C.R. Buhler, J.L. McFall, S.J. Snyder, Particle removal by electrostatic and dielectrophoretic forces for dust control during lunar exploration missions, Journal of Electrostatics. 67 (2009) 89–92. https://doi.org/10.1016/j.elstat.2009.02.012.

[12] P. Atten, H.L. Pang, J. Reboud, Study of dust removal by standing wave electric curtain for application to solar cells on Mars, IEEE Transactions on Industry Applications. 45 (2009) 75–86. https://doi.org/10.1109/TIA.2008.2009723.

[13] H. Kawamoto, M. Uchiyama, B.L. Cooper, D.S. McKay, Mitigation of lunar dust on solar panels and optical elements utilizing electrostatic traveling-wave, Journal of Electrostatics. 69 (2011) 370–379. https://doi.org/10.1016/j.elstat.2011.04.016.

[14] A. Sayyah, R.S. Eriksen, M.N. Horenstein, M.K. Mazumder, Performance analysis of electrodynamic screens based on residual particle size distribution, IEEE Journal of Photovoltaics. 7 (2017) 221–229. https://doi.org/10.1109/JPHOTOV.2016.2617088.

[15] H. Kawamoto, B. Guo, Improvement of an electrostatic cleaning system for removal of dust from solar panels, Journal of Electrostatics. 91 (2018) 28–33. https://doi.org/10.1016/j.elstat.2017.12.002.

[16] B. Guo, B. Figgis, W. Javed, Measurement of electrodynamic dust shield efficiency in field conditions, Journal of Electrostatics. 97 (2019) 26–30. https://doi.org/10.1016/j.elstat.2018.11.007.

[17] S. Masuda, Y. Matsumoto, Theoretical characteristics of standing-wave electric curtains, Electrical Engineering in Japan. 93 (1973) 71–77. https://doi.org/10.1002/eej.4390930110.

[18] S. Masuda, M. Washizu, M. Iwadare, Separation of small particles suspended in liquid by nonuniform traveling field, IEEE Transactions on Industry Applications. IA-23 (1987) 474–480. https://doi.org/10.1109/TIA.1987.4504934.

[19] W.W. Machowski, W. Balachandran, D. Hu, Influence of electrode geometry on transport and separation efficiency of powders using traveling wave field technique, IEEE Transactions on Industry Applications. 33 (1997) 887–892. https://doi.org/10.1109/28.605728.

[20] J.R. Melcher, E.P. Warren, R.H. Kotwal, Traveling-wave delivery of single-component developer, IEEE Transactions on Industry Applications. 25 (1989) 956–961. https://doi.org/10.1109/28.41264.

[21] J.R. Melcher, E.P. Warren, R.H. Kotwal, Theory for finite-phase traveling-wave boundary-guided transport of triboelectrified particles, IEEE Transactions on Industry Applications. 25 (1989) 949–955. https://doi.org/10.1109/28.41263.

[22] J.R. Melcher, E.P. Warren, R.H. Kotwal, Theory for pure-traveling-wave boundary-guided transport of tribo-electrified particles, Particulate Science and Technology. 7 (1989) 1–21. https://doi.org/10.1080/02726358908906520.

[23] A. Sayyah, M.N. Horenstein, M.K. Mazumder, G. Ahmadi, Electrostatic force distribution on an electrodynamic screen, Journal of Electrostatics. 81 (2016) 24–36. https://doi.org/10.1016/j.elstat.2016.02.004.

[24] A. Zouaghi, N. Zouzou, L. Dascalescu, Assessment of forces acting on fine particles on a traveling-wave electric field conveyor: Application to powder manipulation, Powder Technology. 343 (2019) 375–382. https://doi.org/10.1016/j.powtec.2018.11.065.

[25] R. Kober, B. Hill, An experimental setup for bucket brigade toner transport, NIP & Digital Fabrication Conference. 1999 (1999) 258–261.

[26] R. Kober, Traveling wave transport of conductive toner particles, NIP & Digital Fabrication Conference. 2000 (2000) 736–739.

[27] R. Kober, Simulation of traveling wave toner transport, NIP & Digital Fabrication Conference. 2002 (2002) 453–457.

[28] H. Kawamoto, K. Seki, N. Kuromiya, Mechanism of travelling-wave transport of particles, Journal of Physics D: Applied Physics. 39 (2006) 1249. https://doi.org/10.1088/0022-3727/39/6/036.

[29] M.N. Horenstein, M.K. Mazumder, R.C. Sumner, J. Stark, T. Abuhamed, R. Boxman, Modeling of trajectories in an electrodynamic screen for obtaining maximum particle removal efficiency, IEEE Transactions on Industry Applications. 49 (2013) 707–713. https://doi.org/10.1109/TIA.2013.2244192.

[30] Z. Jie, Z. Chuande, Z. Fuzhong, L. Shuhua, F. Miao, T. Yike, Experimental and numerical modeling of particle levitation and movement behavior on traveling-wave electric curtain for particle removal, Particulate Science and Technology. 37 (2019) 737–745. https://doi.org/10.1080/02726351.2018.1438545.

[31] A. Zouaghi, N. Zouzou, Impact of spatial harmonic waves on dielectric particles displacement in standing and traveling wave electric fields, Journal of Electrostatics. 98 (2019) 25–33. https://doi.org/10.1016/j.elstat.2019.01.006.

[32] A. Zouaghi, N. Zouzou, P. Braud, Time Resolved Measurement of Dielectric Particles Velocity on Standing Wave Electric Conveyor using PTV Technique, J. Phys.: Conf. Ser. 1322 (2019) 012034. https://doi.org/10.1088/1742-6596/1322/1/012034.

[33] P. Jiang, H. Bi, S.-C. Liang, L.-S. Fan, Hydrodynamic behavior of circulating fluidized bed with polymeric particles, AIChE Journal. 40 (1994) 193–206. https://doi.org/10.1002/aic.690400202.

[34] M. Pauthenier, M. Moreau-Hanot, La charge des particules sphériques dans un champ ionisé, Journal de Physique et Le Radium. 3 (1932) 590–613.

[35] H.A. Pohl, Dielectrophoresis: the behavior of neutral matter in nonuniform electric fields, Cambridge University Press, Cambridge; New York, 1978.

[36] T.B. Jones, Electromechanics of Particles by Thomas B. Jones, 1995. https://doi.org/10.1017/CBO9780511574498.

[37] D.M. Taylor, P.E. Secker, Industrial electrostatics: fundamentals and measurements, Research Studies Press, 1994.

[38] K.R. Parker, ed., Applied Electrostatic Precipitation, Springer Netherlands, 1997. https://www.springer.com/gp/book/9780751402667 (accessed August 1, 2019).

[39] J.N. Israelachvili, Intermolecular and Surface Forces, Academic Press, 2015.

[40] Y.I. Rabinovich, J.J. Adler, A. Ata, R.K. Singh, B.M. Moudgil, Adhesion between Nanoscale Rough Surfaces: II. Measurement and Comparison with Theory, Journal of Colloid and Interface Science. 232 (2000) 17–24. https://doi.org/10.1006/jcis.2000.7168.

[41] Y.I. Rabinovich, J.J. Adler, M.S. Esayanur, A. Ata, R.K. Singh, B.M. Moudgil, Capillary forces between surfaces with nanoscale roughness, Advances in Colloid and Interface Science. 96 (2002) 213–230. https://doi.org/10.1016/S0001-8686(01)00082-3.

[42] D. Hu, W. Balachandran, W.W. Machowski, Design of traveling-wave field panel for pharmaceutical powders based on computer simulation of particle trajectories, IEEE

Transactions on Industry Applications. 33 (1997) 641–650. https://doi.org/10.1109/28.585853.

[43] Z. Dudzicz, The path of oscillation of dust particles in the field of the electric curtain of the plane type supplied with AC voltage, Journal of Electrostatics. 23 (1989) 207–214. https://doi.org/10.1016/0304-3886(89)90047-8.

[44] Z. Dudzicz, Electrodynamics of charged dust particles and repulsion force within plane-type electric curtain, Journal of Electrostatics. 51–52 (2001) 111–116. https://doi.org/10.1016/S0304-3886(01)00109-7.

[45] A. Zouaghi, N. Zouzou, P. Braud, Study of dielectric particles motion in traveling and standing electrostatic waves using Particle Tracking Velocimetry, J. Phys. D: Appl. Phys. (2020). https://doi.org/10.1088/1361-6463/ab93f6.

FIGURES CAPTIONS

Figure 1. Distribution of electric potential obtained by numerical simulation at $t = 0$ s. Conditions : $V = 1000$ V, $f = 50$ Hz, $\lambda = 6$ mm.

Figure 2. Evolution of electric field vectors at different points $(x, y) = (5, 0.1)$, $(5.5, 0.1)$, $(6, 0.1)$ mm. (a) Total electric field. (b) Forward component of the electric field. (c) Backward component of the electric field. Conditions: $V = 1000$ V, $f = 50$ Hz.

Figure 3. Spatial evolution of the two components of the acceleration a_x and a_y at $t = 0$ s. Conditions : $V = 1000$ V, $f = 100$ Hz, $d_p = 60$ µm, $q_p = 10\ \%\ q_{ps}$ (positive polarity).

Figure 4. Trajectories of particles with different departure positions at (a) 10 ms, (b) 50 ms, (c) 100 ms et (d) 200 ms. Conditions : $V = 1000$ V, $f = 100$ Hz, $d_p = 60$ µm, $q_p = 10\ \%\ q_{ps}$ (positive polarity).

Figure 5. Trajectories of particles obtained experimentally using high speed camera during 200 ms of their motion, the rotary motion can be observed for different particles at different heights. Condition : $V = 1000$ V, $f = 100$ Hz, $d_p[50\ \%] = 57$ µm.

Figure 6. Evolution of horizontal and vertical components of the position and the velocity of a single particle (a) $x_p(t)$, (b) $y_p(t)$, (c) $v_x(t)$, et (d) $v_y(t)$. Conditions : $V = 1000$ V, $f = 100$ Hz, $d_p = 60$ µm, $q_p = 10\ \%\ q_{ps}$ (positive polarity), $x_0 = 6.3$ mm.

Figure 7. Evolution of the particle's levitation height and its displacement distance as a function of the frequency. Conditions : $V = 1000$ V, $d_p = 60$ µm, $q_p = 10\ \%\ q_{ps}$ (positive polarity), $x_0 = 6.3$ mm.

Figure 8. Evolution of the particle's average and maximum velocities as a function of the frequency. Conditions : $V = 1000$ V, $d_p = 60$ µm, $q_p = 10\ \%\ q_{ps}$, $x_0 = 6.3$ mm.

Figure 9. Evolution of the particle position $x_p(t)$ and its instantaneous displacement velocity $v_x(t)$ as a function of time at 5 Hz. Conditions : $V = 1000$ V, $d_p = 60$ µm, $q_p = 10\ \%\ q_{ps}$, $x_0 = 6.3$ mm.

Figure 10. Trajectories obtained for one single particle at different frequency values between 5 Hz and 500 Hz. Conditions : $V = 1000$ V, $d_p = 60$ µm, $q_p = 10\ \%\ q_{ps}$, $x_0 = 6.3$ mm.

Figure 11. Trajectories of particles with (a) 60 µm et (b) 320 µm of diameter under three potential cases: both forward and backward waves, only forward wave, and only backward wave. Conditions : $V = 1000$ V, $f = 100$ Hz, $q_p = 10\ \%\ q_{ps}$, $x_0 = 6.3$ mm.

Figure 12. Variation of the displacement distance of the particles as the function of the frequency under three potential cases: both forward and backward waves, only forward wave, and only backward wave. Conditions : $V = 1000$ V, $f = 100$ Hz, $d_p = 60$ µm, $q_p = 10\ \%\ q_{ps}$, $x_0 = 6.3$ mm.

Figure 13. Characteristic $v_{x-avg}(f)$ of the particle under three potential cases: both forward and backward waves, only forward wave, and only backward wave. Conditions : $V = 1000$ V, $f = 100$ Hz, $d_p = 60$ µm, $q_p = 10\ \%\ q_{ps}$, $x_0 = 6.3$ mm.

Figure 1

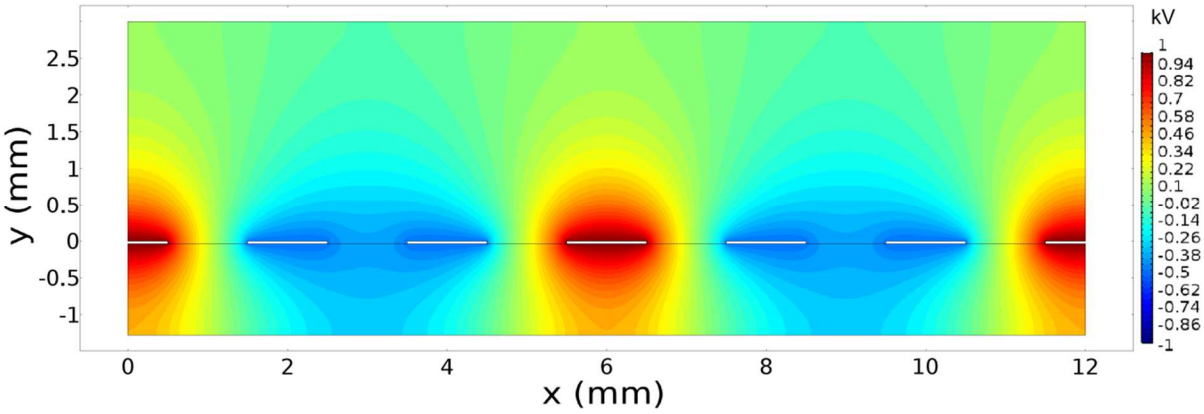
kV
1
0.94
0.82
0.7
0.58
0.46
0.34
0.22
0.1
-0.02
-0.14
-0.26
-0.38
-0.5
-0.62
-0.74
-0.86
-1
y (mm)
2.5
2
1.5
1
0.5
0
-0.5
-1
0
2
4
6
8
10
12
x (mm)

Figure 2

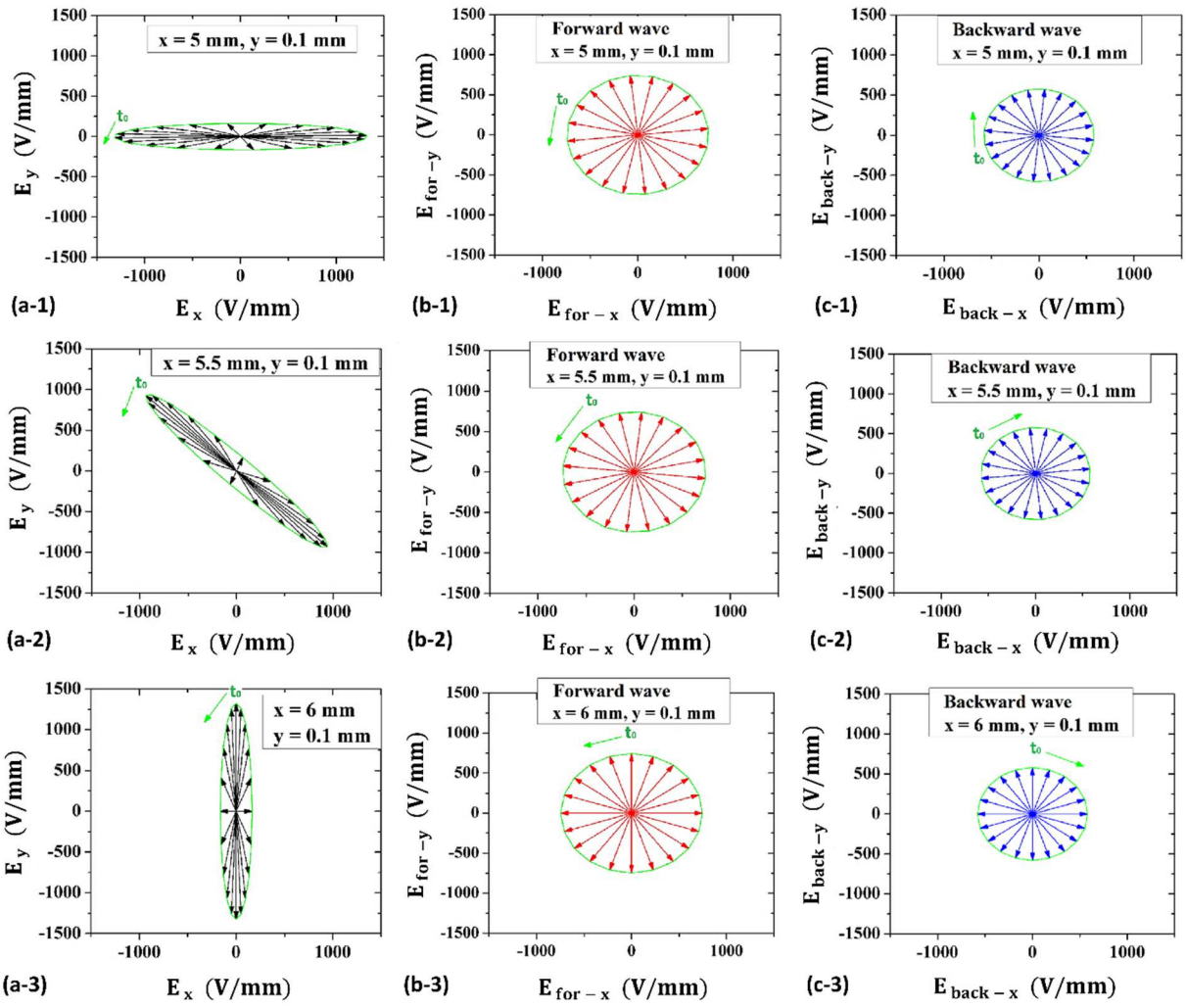
x = 5 mm, y = 0.1 mm
Forward wave
x = 5 mm, y = 0.1 mm
Backward wave
x = 5 mm, y = 0.1 mm
x = 5.5 mm, y = 0.1 mm
Forward wave
x = 5.5 mm, y = 0.1 mm
Backward wave
x = 5.5 mm, y = 0.1 mm
x = 6 mm
y = 0.1 mm
Forward wave
x = 6 mm, y = 0.1 mm
Backward wave
x = 6 mm, y = 0.1 mm
t0
E y (V/mm)
E for –y (V/mm)
E back –y (V/mm)
E x (V/mm)
E for – x (V/mm)
E back – x (V/mm)
1500
1000
500
0
-500
-1000
-1500
-1000
0
1000
(a-1)
(b-1)
(c-1)
(a-2)
(b-2)
(c-2)
(a-3)
(b-3)
(c-3)

Figure 3

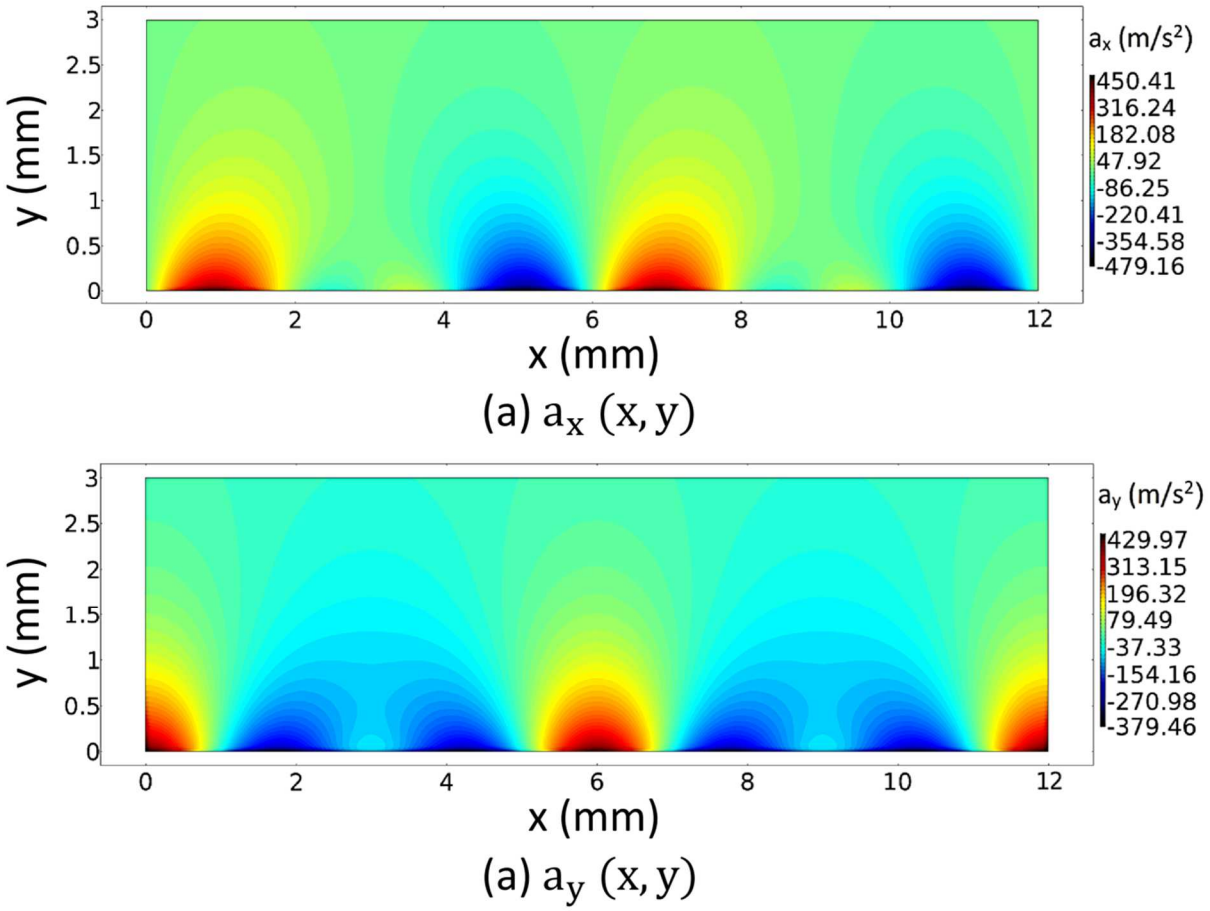
y (mm)
x (mm)
a_x (m/s²)
450.41
316.24
182.08
47.92
-86.25
-220.41
-354.58
-479.16
(a) a_x (x, y)
y (mm)
x (mm)
a_y (m/s²)
429.97
313.15
196.32
79.49
-37.33
-154.16
-270.98
-379.46
(a) a_y (x, y)

Figure 4

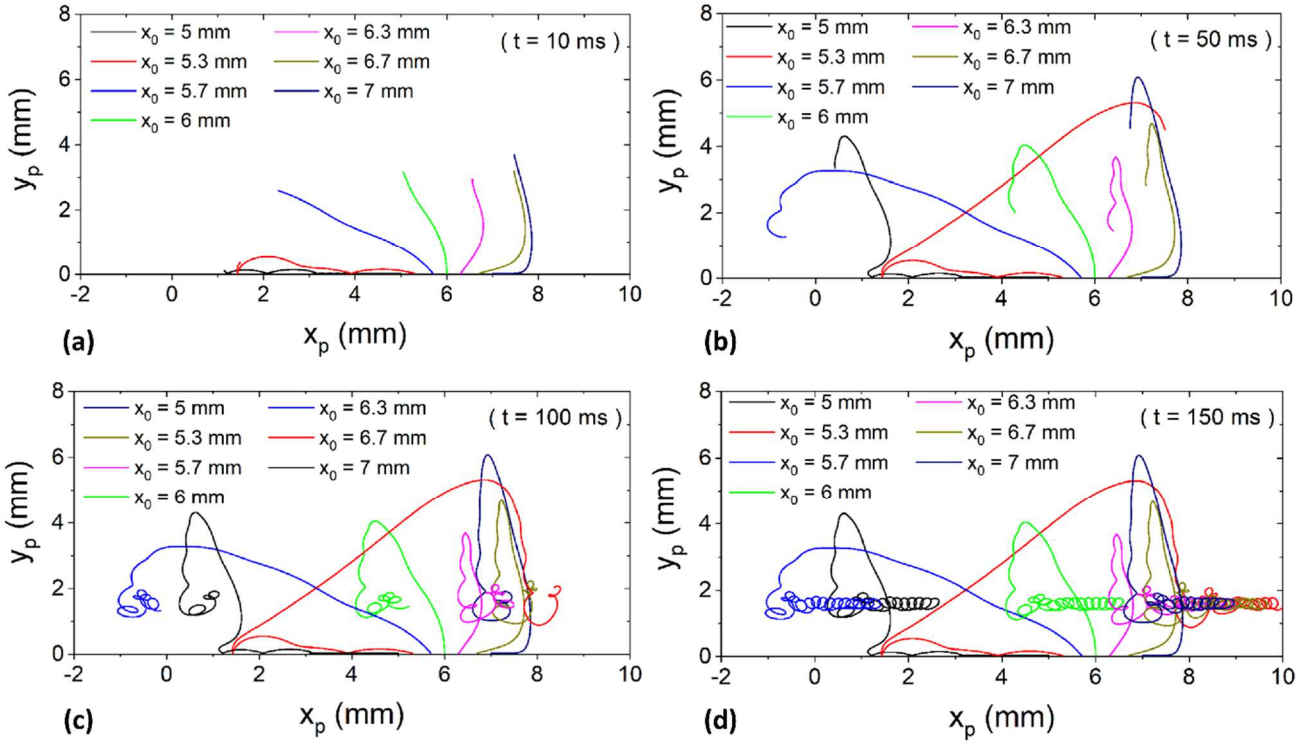
x0 = 5 mm
x0 = 5.3 mm
x0 = 5.7 mm
x0 = 6 mm
x0 = 6.3 mm
x0 = 6.7 mm
x0 = 7 mm
(t = 10 ms)
(t = 50 ms)
(t = 100 ms)
(t = 150 ms)
yp (mm)
xp (mm)
(a)
(b)
(c)
(d)

Figure 5

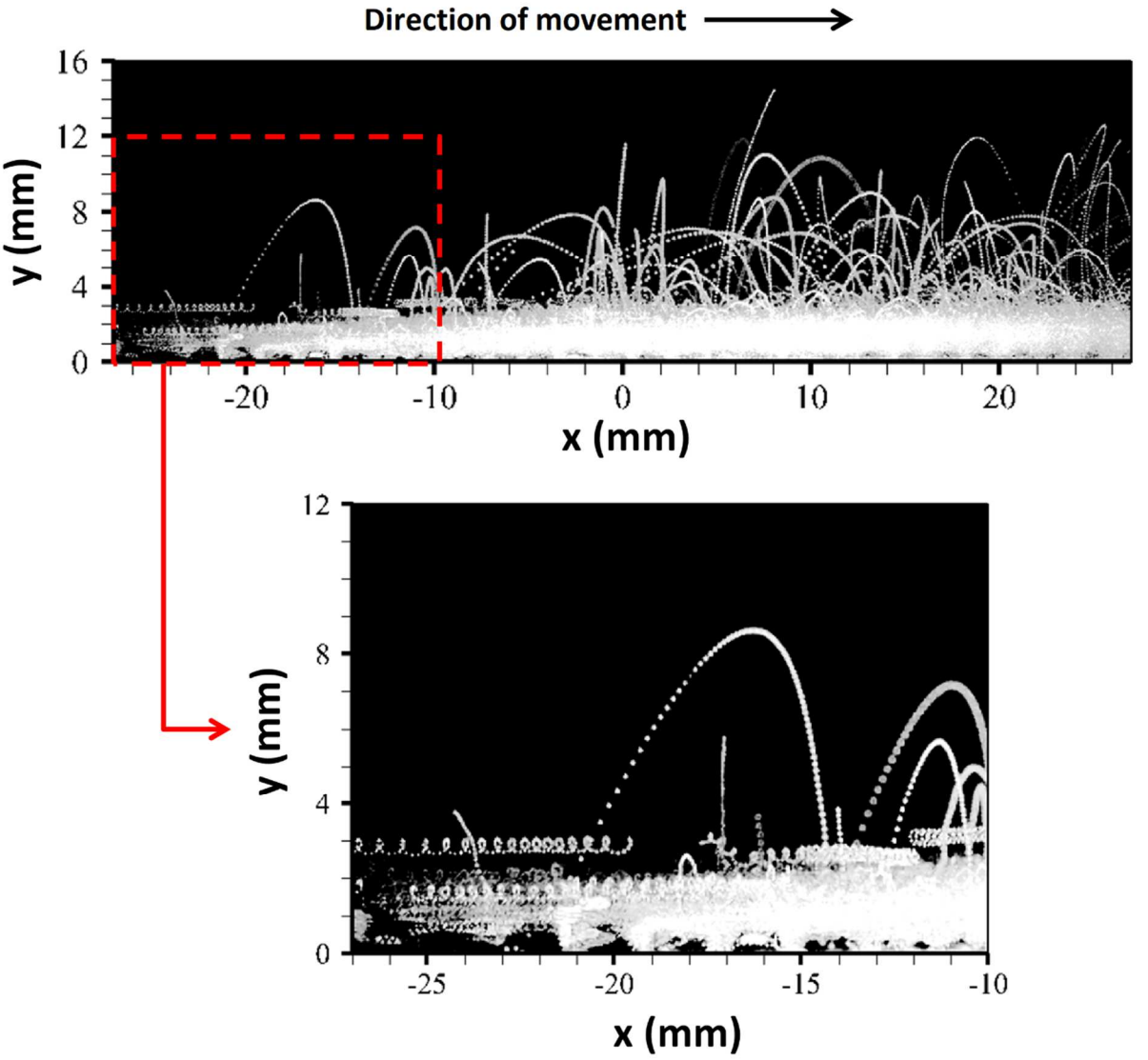
Direction of movement
16
12
8
4
0
y (mm)
-20
-10
0
10
20
x (mm)
12
8
4
0
y (mm)
-25
-20
-15
-10
x (mm)

Figure 6

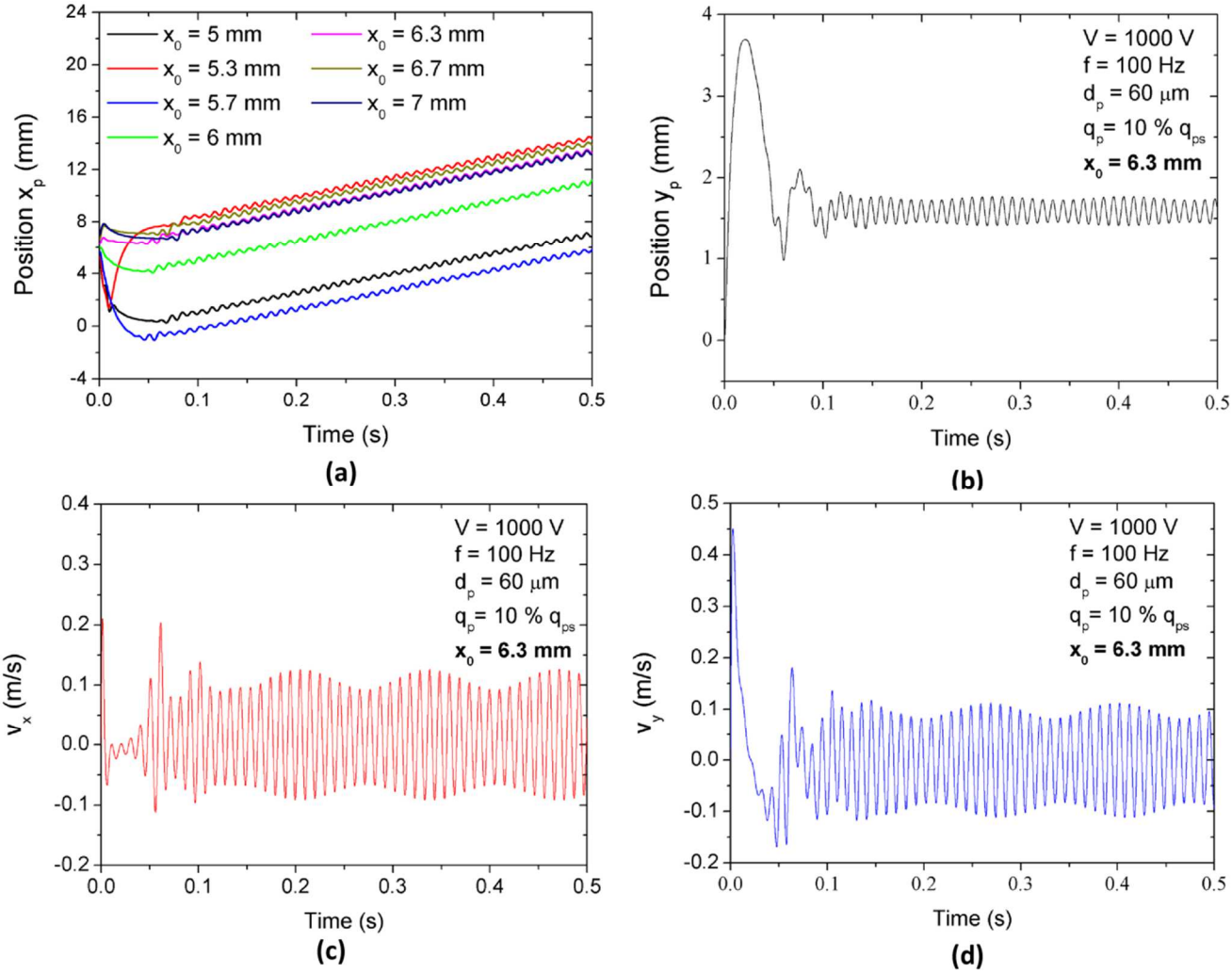
x0 = 5 mm
x0 = 5.3 mm
x0 = 5.7 mm
x0 = 6 mm
x0 = 6.3 mm
x0 = 6.7 mm
x0 = 7 mm
Position xp (mm)
Time (s)
(a)
V = 1000 V
f = 100 Hz
dp = 60 μm
qp= 10 % qps
x0 = 6.3 mm
Position yp (mm)
Time (s)
(b)
vx (m/s)
Time (s)
(c)
vy (m/s)
Time (s)
(d)

Figure 7

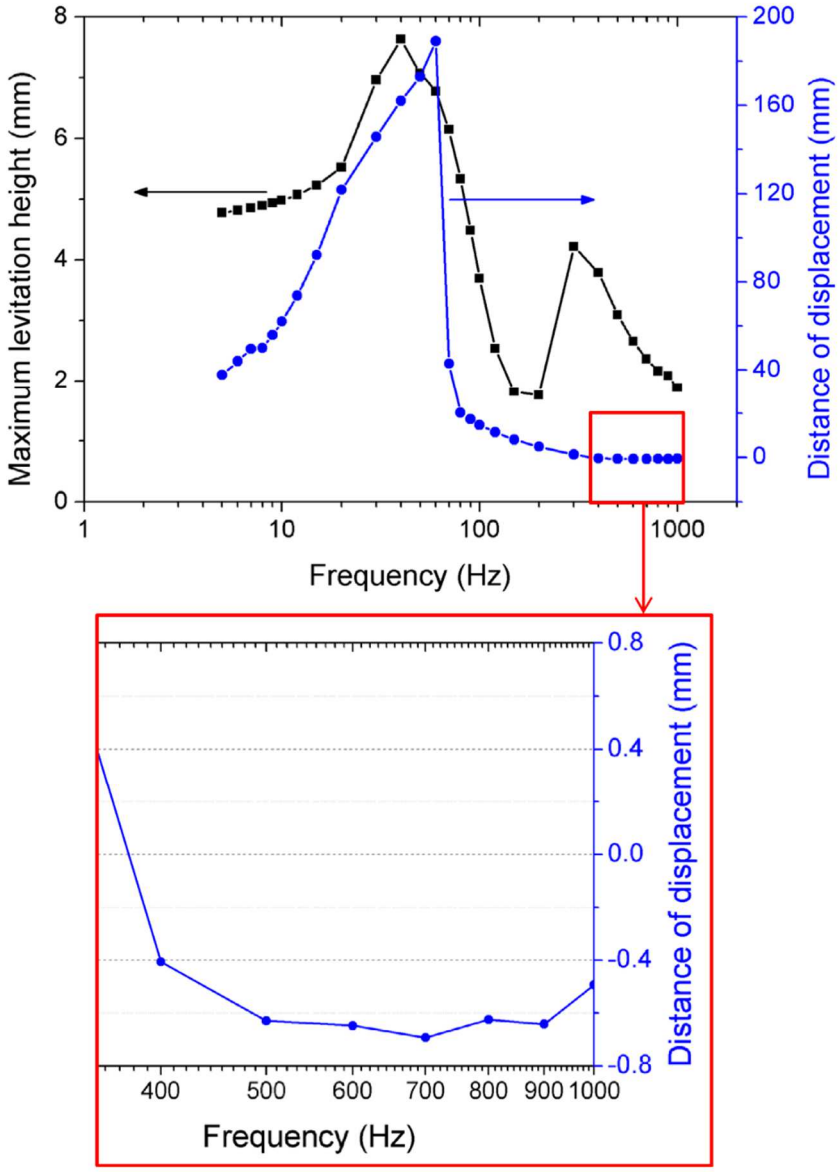
Maximum levitation height (mm)
Distance of displacement (mm)
Frequency (Hz)
0
2
4
6
8
0
40
80
120
160
200
1
10
100
1000
0.8
0.4
0.0
-0.4
-0.8
400
500
600
700
800
900
1000

Figure 8

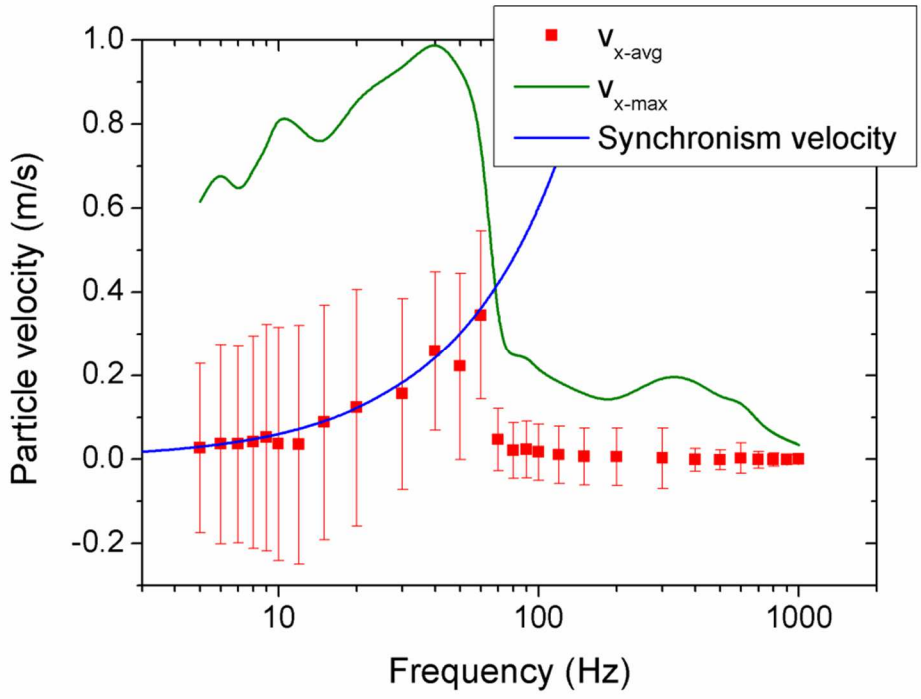
1.0
0.8
0.6
0.4
0.2
0.0
-0.2
Particle velocity (m/s)
10
100
1000
Frequency (Hz)
v x-avg
v x-max
Synchronism velocity

Figure 9

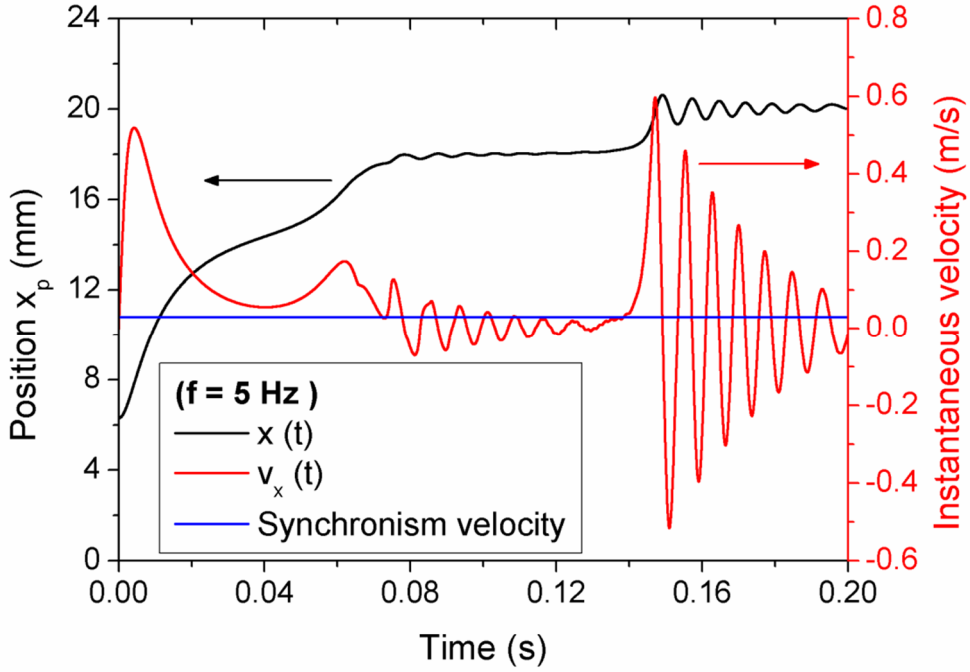
Position x_p (mm)
Instantaneous velocity (m/s)
Time (s)
(f = 5 Hz)
x (t)
v_x (t)
Synchronism velocity
0
4
8
12
16
20
24
-0.6
-0.4
-0.2
0.0
0.2
0.4
0.6
0.8
0.00
0.04
0.08
0.12
0.16
0.20

Figure 10

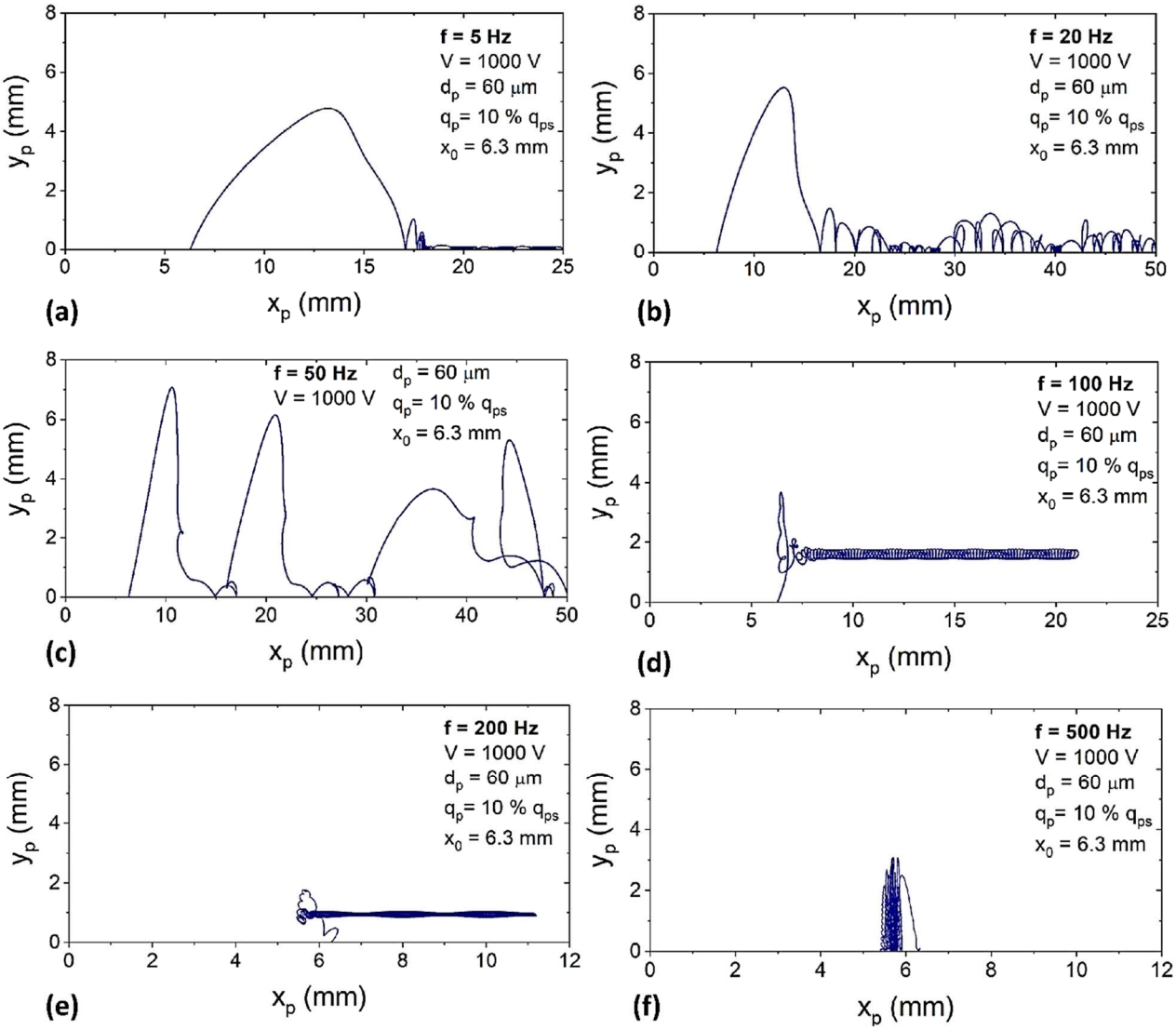
f = 5 Hz
V = 1000 V
d_p = 60 μm
q_p= 10 % q_{ps}
x_0 = 6.3 mm
(a)
f = 20 Hz
V = 1000 V
d_p = 60 μm
q_p= 10 % q_{ps}
x_0 = 6.3 mm
(b)
f = 50 Hz
V = 1000 V
d_p = 60 μm
q_p= 10 % q_{ps}
x_0 = 6.3 mm
(c)
f = 100 Hz
V = 1000 V
d_p = 60 μm
q_p= 10 % q_{ps}
x_0 = 6.3 mm
(d)
f = 200 Hz
V = 1000 V
d_p = 60 μm
q_p= 10 % q_{ps}
x_0 = 6.3 mm
(e)
f = 500 Hz
V = 1000 V
d_p = 60 μm
q_p= 10 % q_{ps}
x_0 = 6.3 mm
(f)
y_p (mm)
x_p (mm)

Figure 11

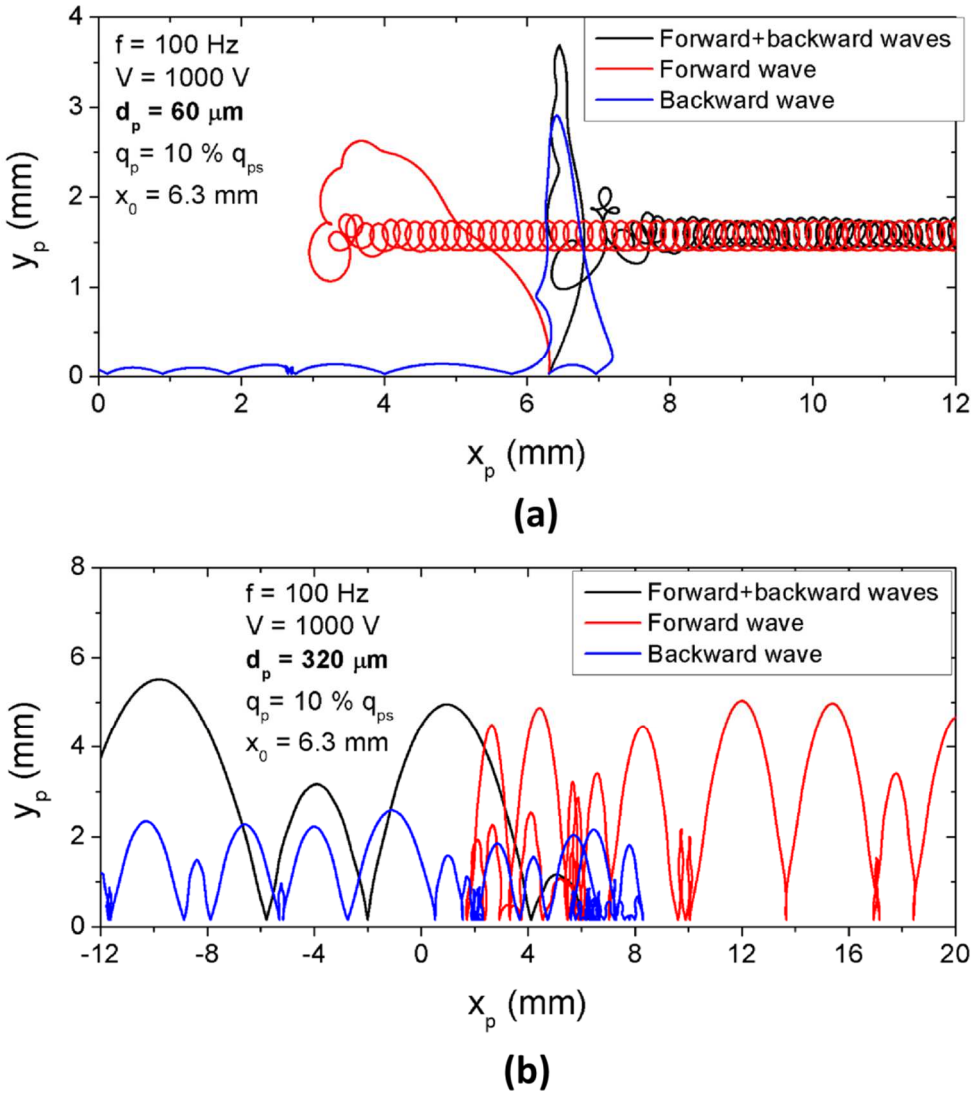
f = 100 Hz
V = 1000 V
d_p = 60 μm
q_p = 10 % q_ps
x_0 = 6.3 mm
Forward+backward waves
Forward wave
Backward wave
y_p (mm)
x_p (mm)
(a)
f = 100 Hz
V = 1000 V
d_p = 320 μm
q_p = 10 % q_ps
x_0 = 6.3 mm
Forward+backward waves
Forward wave
Backward wave
y_p (mm)
x_p (mm)
(b)

Figure 12

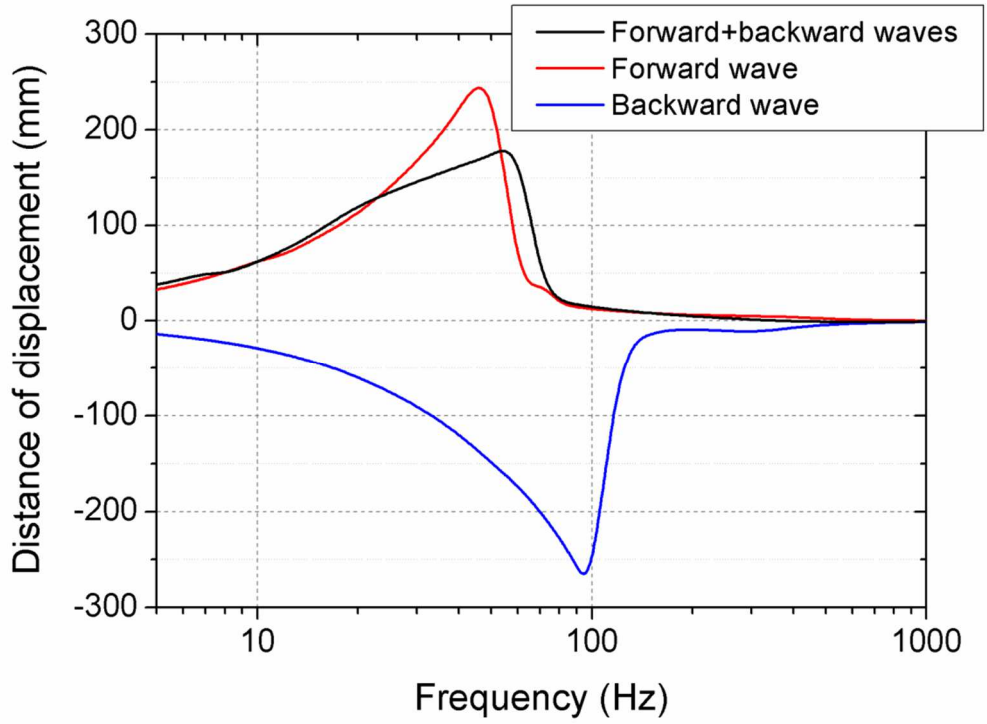
Forward+backward waves
Forward wave
Backward wave
Distance of displacement (mm)
300
200
100
0
-100
-200
-300
10
100
1000
Frequency (Hz)

Figure 13

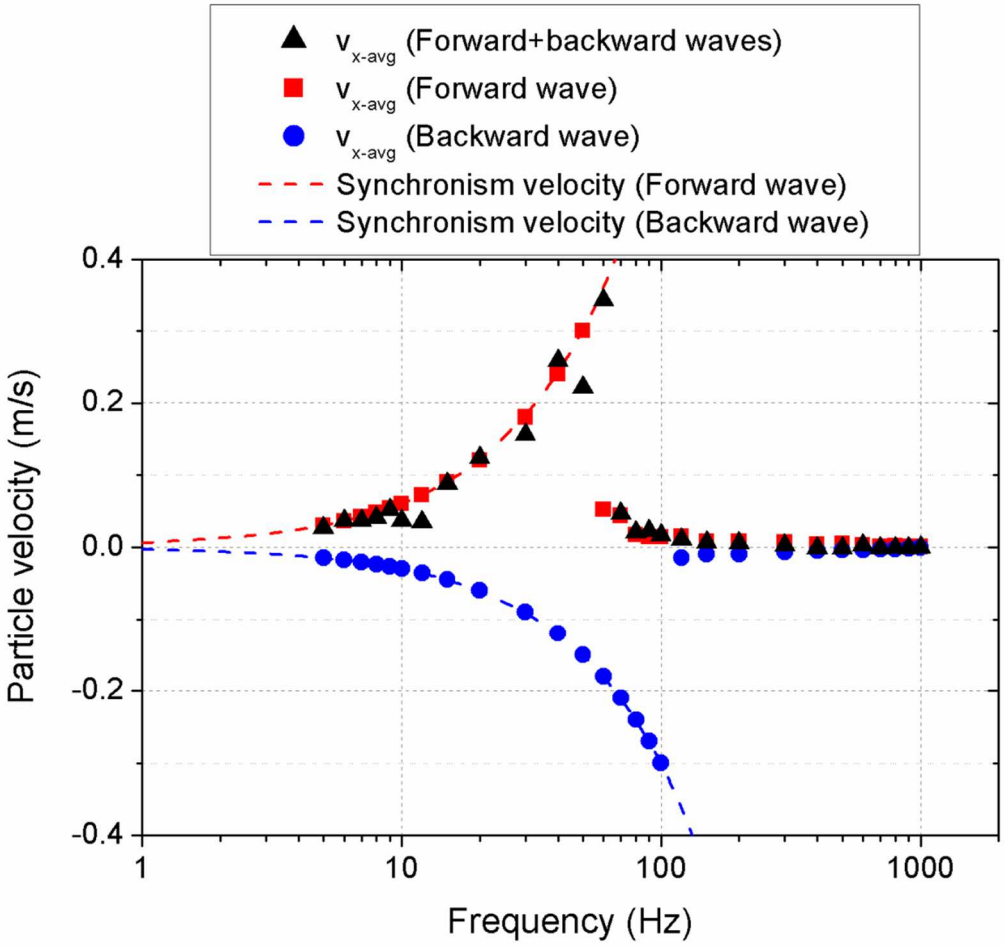
v x-avg (Forward+backward waves)
v x-avg (Forward wave)
v x-avg (Backward wave)
Synchronism velocity (Forward wave)
Synchronism velocity (Backward wave)
Particle velocity (m/s)
0.4
0.2
0.0
-0.2
-0.4
1
10
100
1000
Frequency (Hz)